



# Effect of Zr Addition on Microstructure and Mechanical Properties of a Cast Cu<sub>60</sub>Fe<sub>40</sub> Alloy

Jongun Moon<sup>1</sup> · Eun Seong Kim<sup>1</sup> · Yeon Taek Choi<sup>1</sup> · Ho-Joon Moon<sup>2</sup> · Jung-Wook Cho<sup>2</sup> · Hyoung Seop Kim<sup>1,2,3,4</sup>

Received: 2 September 2022 / Accepted: 30 September 2022 / Published online: 9 October 2022  
© The Author(s) under exclusive licence to The Korean Institute of Metals and Materials 2022

## Abstract

Cu–Fe alloys have drawn extensive attraction due to excellent multi-functional properties, including electrical, magnetic, and mechanical properties. However, the immiscible nature of Cu–Fe alloys results in heterogeneous microstructure and unexpected mechanical properties. In this study, a small amount of Zr was added to the cast Cu<sub>60</sub>Fe<sub>40</sub> (wt%) alloy to suppress the liquid–liquid phase separation during solidification of the alloy. The microstructure and mechanical properties of the Zr-free and Zr-containing Cu–Fe alloy were investigated. It is found that the addition of Zr successfully inhibits the heterogeneous microstructural evolution caused by liquid–liquid phase separation, while the FeZr-rich precipitates form in the dual-phase microstructure. The FeZr-rich precipitates affect grain growth of the Zr-containing alloy through the Zener pinning effect, leading to extra grain boundary strengthening and precipitation hardening. The resulting microstructure of the Zr-containing alloy substantially enhances the strength of the alloy with a loss of ductility. The fractured surface reveals that microcracks are formed near the precipitates, which is associated with the reduced elongation of the Zr-containing alloy.

**Keywords** Cu–Fe alloys · Liquid–liquid phase separation · Dual-phase · Mechanical properties · Precipitation hardening

## 1 Introduction

Binary Cu–Fe alloys are known as immiscible alloys that separate the microstructure into Cu-rich and Fe-rich regions due to their high mixing enthalpy [1, 2]. The dual-phase microstructure in the Cu–Fe system with the coexistence of body-centered cubic (BCC) Fe-rich and face-centered cubic (FCC) Cu-rich phases can lead to high electrical conductivity [3–5], electromagnetic shielding [6], excellent magnetic

properties [7, 8], and good mechanical properties [9–11]. As an exemplar, the Cu<sub>70</sub>Fe<sub>30</sub> (wt%) alloy fabricated by powder metallurgy and cold-rolling exhibits a good combination of electrical and magnetic properties with electrical conductivity of 50.2% IACS, magnetic saturation strength of 60.39 emu·g<sup>-1</sup>, and coercivity of 98.2 Oe owing to its unique Cu–Fe composite structure [5]. Interestingly, in Cu-based alloys such as Cu–Fe [12], Cu–Co [13], and Cu–Cr [14], there is a liquid miscibility gap in their phase diagram, which results in liquid–liquid phase separation (LLPS) into droplet-shaped liquid phases during solidification. However, LLPS commonly produces fatal and detrimental influences on the homogeneity of microstructure and mechanical properties [15, 16]. Thus, the microstructural features of LLPS have been avoided by adjusting cooling rate [17–19] and chemical composition [20].

Recently, Moon et al. [21] proposed a pathway to prevent the occurrence of LLPS in cast Cu<sub>60</sub>Fe<sub>40</sub> and Cu<sub>80</sub>Fe<sub>20</sub> (wt%) alloys by adding 1 wt% of Zr. It should be noted that Zr element possesses a negative mixing enthalpy with both Cu and Fe, which in turn, decreases the overall Gibbs free energy of mixing [21]. After adding a small amount of Zr into the Cu–Fe alloys, the degree of supercooling was substantially reduced and the heterogeneous nucleation of  $\gamma$ -Fe

✉ Hyoung Seop Kim  
hskim@postech.ac.kr

<sup>1</sup> Department of Materials Science and Engineering, Pohang University of Science and Technology (POSTECH), Pohang 37673, Republic of Korea  
<sup>2</sup> Graduate Institute of Ferrous and Energy Materials Technology, Pohang University of Science and Technology (POSTECH), Pohang 37673, Republic of Korea  
<sup>3</sup> Center for Heterogeneous Metal Additive Manufacturing, Pohang University of Science and Technology (POSTECH), Pohang 37673, Republic of Korea  
<sup>4</sup> Institute for Convergence Research and Education in Advanced Technology, Yonsei University, Seoul 03722, Republic of Korea

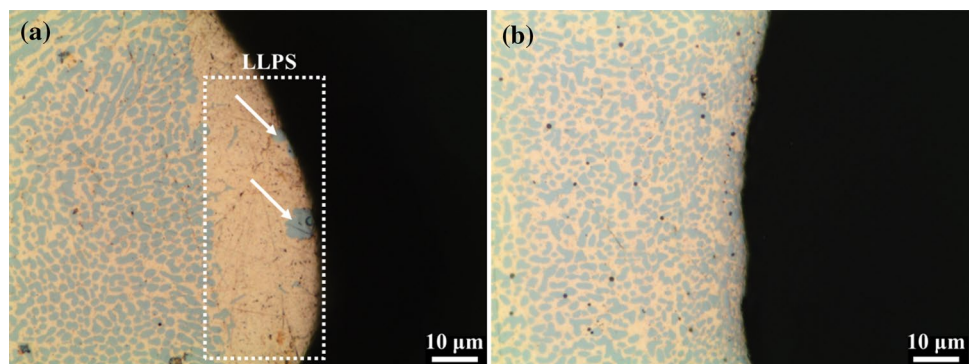
was accelerated during solidification [21]. Consequently, LLPS was eliminated and a relatively homogeneous microstructure was achieved in the Zr-containing Cu–Fe alloys [21]. Meantime, although the Zr addition successfully settled a problem associated with the non-uniform microstructure caused by LLPS of Cu–Fe alloys, the precipitation of intermetallic compounds in the ternary Cu–Fe–Zr system can raise another challenge on the mechanical properties of alloys. According to the phase diagrams of binary Cu–Zr and Fe–Zr [22, 23], the solubility of Zr in Cu and Fe is extremely limited. It is anticipated that the Zr addition to the Cu–Fe system may lead to the formation of Zr-enriched precipitates in its microstructure. Hence, in order to disclose the development potential of Zr-containing Cu–Fe alloys, the relationship between the microstructure and mechanical properties of the alloys is required to be elucidated.

In this study, we investigated the microstructural evolution and mechanical properties of cast  $\text{Cu}_{60}\text{Fe}_{40}$  and  $\text{Cu}_{59.4}\text{Fe}_{39.6}\text{Zr}_1$  (wt%) alloys. The addition of Zr to a Cu–Fe alloy influences the LLPS behavior, grain growth, and formation of a considerable amount of  $\text{Fe}_2\text{Zr}$ -type precipitates. The strength of the Zr-containing alloy is remarkably improved compared to the Zr-free alloy through grain refinement and precipitation hardening, whereas the elongation of the alloy is inevitably deteriorated. The fractography of the alloys reveals that microcracks are generated near  $\text{Fe}_2\text{Zr}$ -type precipitates during failure, which reduces the elongation of the Zr-containing alloy.

## 2 Materials and Methods

Cylindrical  $\text{Cu}_{60}\text{Fe}_{40}$  and  $\text{Cu}_{59.4}\text{Fe}_{39.6}\text{Zr}_1$  (wt%) ingots were fabricated using a vacuum induction melter (VTC-200 V, Indutherm) in an Ar atmosphere inside a graphite mold. The purity of Cu, Fe, and Zr elements used for casting was above 99.5%. The dimensions of the cylindrical ingots were 30 mm in diameter and 90 mm in height. Hereinafter, as-cast  $\text{Cu}_{60}\text{Fe}_{40}$  and  $\text{Cu}_{59.4}\text{Fe}_{39.6}\text{Zr}_1$  alloys are referred to as CF and CFZ, respectively.

**Fig. 1** OM images of the **a** CF and **b** CFZ alloys. The red and blue phases in **a**, **b** are Cu-rich and Fe-rich phases, respectively. The droplet-shaped Fe-rich phase is indicated by the white arrows in **a**



Microstructural characterization of the alloys was performed using X-ray diffraction (XRD), optical microscope (OM), and scanning electron microscope (SEM). XRD measurements of the as-cast alloys were conducted using Bruker D8 Advance XRD equipment with the incident beam of Cu  $K\alpha$  radiation (wavelength = 1.5418 Å). The surfaces of the XRD specimens were finely polished with up to 1  $\mu\text{m}$  diamond suspension in order to reduce surface roughness. The XRD scans were performed with a step size of  $0.02^\circ$  and a scan speed of  $1^\circ/\text{min}$ . OM analysis was performed using an Olympus BX51M equipment. SEM characterization was conducted using Phillips XL30S FEG and FEI Quanta 3D FEG devices with back-scattered electron (BSE), electron backscatter diffraction (EBSD), and energy dispersive spectroscopy (EDS) detectors. EBSD measurements were performed using TSL/OIM software with a step size of 200 nm and the obtained EBSD data were analyzed using TSL/OIM. Specimens for OM and SEM were prepared by polishing with SiC paper up to 1200-grit, followed by grinding with 3 and 1  $\mu\text{m}$  diamond suspensions, and finally with colloidal silica suspension for 30 min. The fraction of precipitates was determined using an ImageJ software.

Tensile tests were conducted using an Instron 1361 machine with a strain rate of  $10^{-3} \text{ s}^{-1}$  at room temperature. The tensile testing was performed using a dog-bone shaped tensile specimen with a gauge length of 1.5 mm, a width of 1.0 mm, and a thickness of 1.0 mm. The surfaces of tensile specimens were polished with up to 1200-grit SiC papers before tensile testing. Each tensile test was repeated at least three times to ensure the reliability of the tests. During the tensile tests, the engineering strains were carefully measured using a digital image correlation (DIC) method.

## 3 Results and Discussion

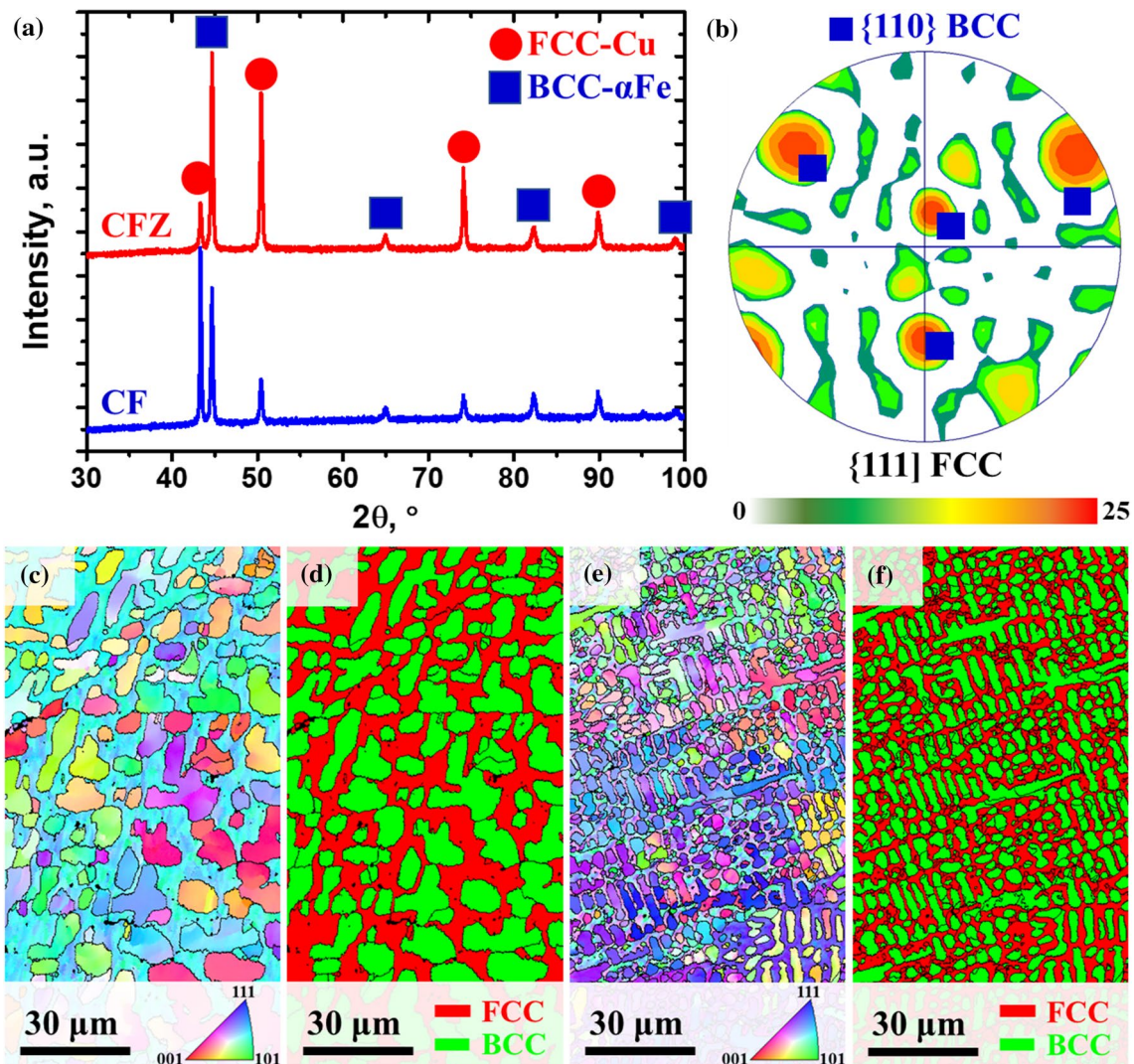
### 3.1 Microstructures

Figure 1 shows the microstructure of the as-cast CF and CFZ alloys. It is clearly seen that the droplet-shaped Fe-rich phase

is formed in the Cu-rich region of the CF alloy as an outcome of LLPS. On a contrary, there is no trace of the LLPS in the CFZ alloy, which leads to a relatively homogeneous Cu–Fe dual-phase microstructure (Fig. 1b). The samples in Fig. 1 were taken near the surface of a cylindrical ingot where the cooling rate during solidification is faster than the center. According to the previous work [21], the addition of a small amount of Zr to the Cu–Fe alloys promotes a reduction in the Gibbs free energy of mixing accompanied by a low degree of supercooling, which leads to a bypass of LLPS during the solidification path and the occurrence of heterogeneous nucleation of  $\gamma$ -Fe. Thus, in the CFZ alloy, the droplet-shaped phase is eliminated due to the restrained LLPS behavior.

The XRD patterns of the CF and CFZ alloys reveal that the alloys mainly consist of Cu-rich FCC and Fe-rich

BCC phases (Fig. 2a). The pole figure of the CF alloy in Fig. 2b shows that the Cu-rich FCC and Fe-rich BCC phases are expected to possess the orientation relationships, such as Kurdjumov-Sachs (K-S) ( $\{111\}$ FCC// $\{011\}$ BCC,  $\langle 011 \rangle$ FCC// $\langle 111 \rangle$ BCC) [24] or Nishiyama-Wassermann (N-W) ( $\{111\}$ FCC// $\{011\}$ BCC,  $\langle 112 \rangle$ FCC// $\langle 011 \rangle$ BCC) [25, 26]. The distinct dual-phase microstructure of the alloys is disclosed in the EBSD inverse pole figure (IPF) and phase maps, as shown in Fig. 2c–f. The phase fractions and average grain sizes of the Cu-rich FCC and Fe-rich BCC phases are summarized in Table 1. After the Zr addition, the fraction of the Fe-rich BCC phase slightly decreases, while the average grain size of both phases for CFZ alloy decreases compared to the Zr-free CF alloy. Note that the average grain size of each phase may be underestimated due to interference caused by the co-existence of the dual-phase.



**Fig. 2** a XRD patterns of the CF and CFZ alloys. b  $\{111\}$  FCC pole figure superimposed with  $\{110\}$  BCC (blue squares) in CF alloy. EBSD-IPF and phase maps of the c, d CF and e, f CFZ alloys



**Table 1** Phase fraction and average grain size of each phase of the alloys

Alloys	Phase fraction, %		Grain size, $\mu\text{m}$	
	Cu-rich FCC	Fe-rich BCC	Cu-rich FCC	Fe-rich BCC
CF	44.2	55.8	$9.6 \pm 3.4$	$10.9 \pm 4.6$
CFZ	47.7	52.3	$4.6 \pm 2.4$	$6.0 \pm 4.3$

Figure 3 shows the FeZr-rich precipitates observed within the Cu-rich region of the CFZ alloy. The chemical compositions of each region of the CF and CFZ alloys are listed in Table 2. It should be noted that the Fe content in the Cu-rich region is higher in the CFZ alloy compared to the CF alloy. During solidification of the CFZ alloy, LLPS disappears and  $\gamma$ -Fe nucleation precedes binodal decomposition [21]. This may result in solute trapping of Fe in the Cu-rich region, which increases the Fe content in the Cu-rich region of the CFZ alloy. Accordingly, excessive dissolution of Fe within the Cu-rich region contributes to the lower fraction of Fe-rich BCC phase in the CFZ alloy (Table 2). Furthermore, the formation of FeZr-rich precipitates is attributed to the high Fe content inside the Cu-rich region of the CFZ alloy. Most of the Zr content of the alloy is consumed in the formation of the FeZr-rich precipitates, as shown in Table 2. According to the chemical composition of the precipitate, the precipitate is found to be  $\text{Fe}_2\text{Zr}$ -type, which is a typical precipitate in the Fe-Zr binary system [27]. The areal fraction of the precipitates is  $4.7 \pm 1.7\%$ , while the mean equivalent radius of the precipitates is  $\sim 700$  nm. It is worth noting that the grain

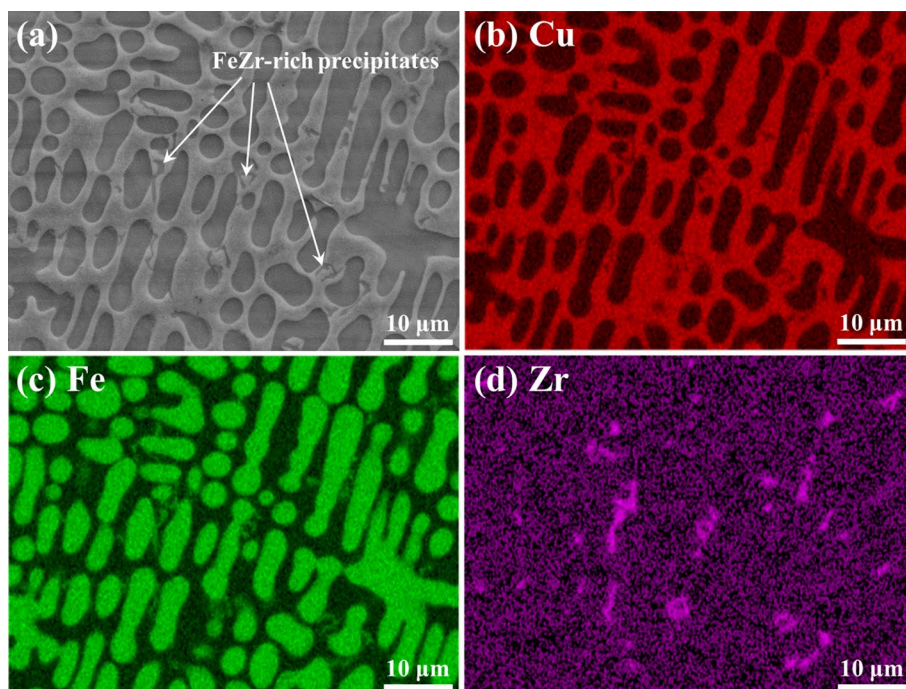
**Table 2** Chemical compositions of each region of the alloys determined by EDS

Regions	Alloys	Chemical composition, wt%		
		Cu	Fe	Zr
Overall	CF	$61.1 \pm 0.3$	$38.9 \pm 0.3$	–
	CFZ	$56.1 \pm 1.1$	$43.3 \pm 1.1$	$0.6 \pm 0.1$
Cu-rich FCC	CF	$94.3 \pm 5.7$	$5.7 \pm 2.6$	–
	CFZ	$90.4 \pm 9.5$	$9.5 \pm 5.0$	$0.1 \pm 0.1$
Fe-rich BCC	CF	$13.7 \pm 0.6$	$86.3 \pm 0.6$	–
	CFZ	$13.9 \pm 0.3$	$86.0 \pm 0.4$	$0.1 \pm 0.1$
Precipitate	CF	–	–	–
	CFZ	$44.85 \pm 8.88$	$35.47 \pm 6.07$	$19.68 \pm 3.90$

growth may be suppressed due to the Zener pinning effect of the  $\text{Fe}_2\text{Zr}$  precipitates in the CFZ alloy [28]. Consequently, the average grain size of the CFZ alloy is smaller than that of the CF alloy.

### 3.2 Mechanical Properties

The tensile properties of the alloys are shown in Fig. 4. The yield and ultimate tensile strengths were improved substantially from  $303 \pm 5$  and  $497 \pm 11$  in the CF alloy to  $506 \pm 22$  and  $645 \pm 7$  in the CFZ alloy, respectively. Meantime, the uniform elongation slightly reduces from  $13 \pm 1\%$  in the CF alloy to  $9 \pm 1\%$  in the CFZ alloy. It should be noted that the total elongation of the CFZ alloy drastically decreases by  $\sim 18\%$  compared to that of the CF alloy. Figure 5 shows

**Fig. 3** a SEM-BSE image of the CFZ alloy and the corresponding EDS maps of b Cu, c Fe, and d Zr

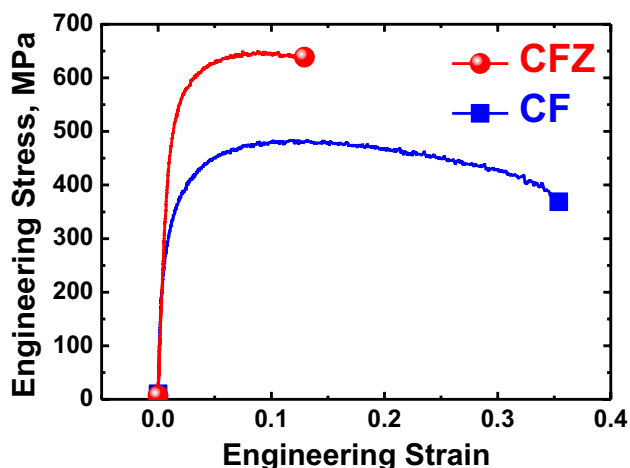


Fig. 4 Engineering stress–strain curves of the alloys

the fractured surfaces of the CF and CFZ alloys after tensile deformation. As shown in Fig. 5a, a typical ductile failure with dimples is observed in the CF alloy. Despite the dimpled structure is also observed in the CFZ alloy in Fig. 5b, the size of the dimples is reduced in the CFZ alloy compared to the CF alloy, which is attributed to the smaller grain size in the Zr-containing alloy [29]. Moreover, a microcrack appears near the Fe<sub>2</sub>Zr precipitates (Fig. 5c, d). Hence, the limited deformation capability due to the smaller grain size and the formation of microcracks at the matrix/precipitate

boundary is responsible for the deteriorated elongation of the CFZ alloy compared to the CF alloy.

### 3.3 Strengthening Mechanisms

The improved strength of the CFZ alloy is associated with the reduced grain size and the formation of Fe<sub>2</sub>Zr precipitates in its microstructure. The strength enhancement ( $\Delta\sigma$ ) between the current alloys can be expressed as follows:

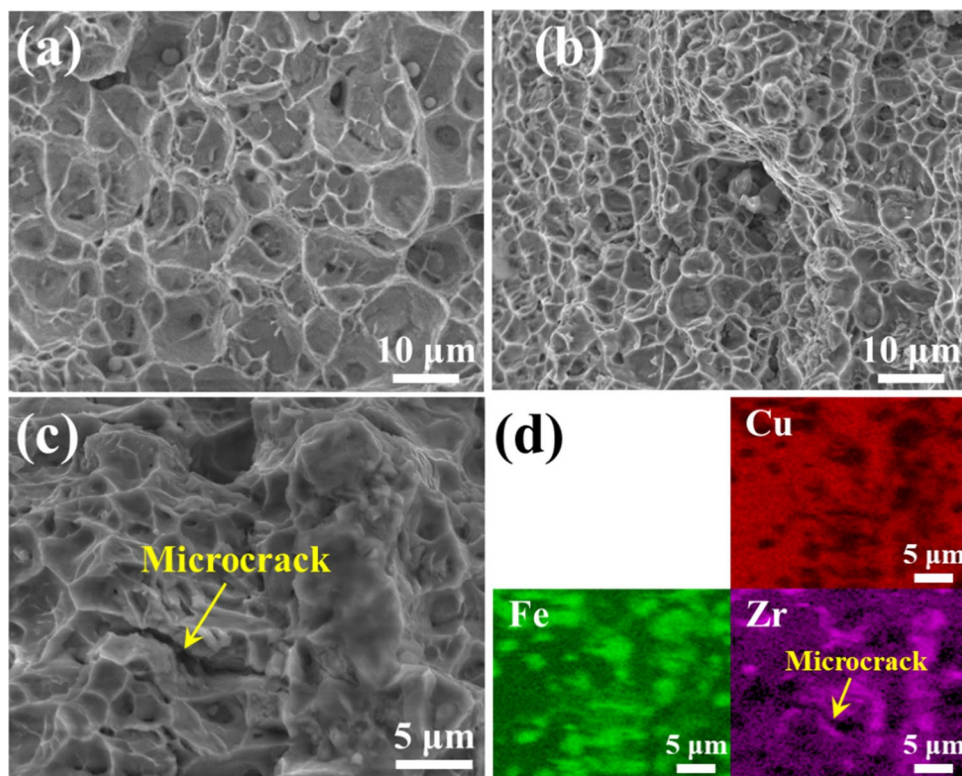
$$\Delta\sigma = \Delta\sigma_{gb} + \Delta\sigma_{ppt}, \tag{1}$$

where  $\Delta\sigma_{gb}$  and  $\Delta\sigma_{ppt}$  are the strength enhancement caused by grain boundaries and precipitates, respectively. The  $\Delta\sigma_{gb}$  is determined by:

$$\Delta\sigma_{gb} = f_{Cu}K_{H-P}^{Cu} \left( d_{CFZ}^{Cu-1/2} - d_{CF}^{Cu-1/2} \right) + f_{Fe}K_{H-P}^{Fe} \left( d_{CFZ}^{Fe-1/2} - d_{CF}^{Fe-1/2} \right), \tag{2}$$

where  $f_{Cu}$ ,  $f_{Fe}$ ,  $K_{H-P}^{Cu}$ , and  $K_{H-P}^{Fe}$  are the fractions ( $f$ ) and the Hall–Petch coefficients ( $K$ ) of the Cu-rich and Fe-rich phases, respectively. The terms,  $d_{CF}^{Cu}$ ,  $d_{CF}^{Fe}$ ,  $d_{CFZ}^{Cu}$ , and  $d_{CFZ}^{Fe}$ , are the grain size of each phase in the CF and CFZ alloys, respectively. The Hall–Petch coefficients of each phase in the alloys are adopted from the values of  $K$  for interstitial-free steel ( $488 \text{ MPa}\cdot\mu\text{m}^{1/2}$ ) [30] and Cu<sub>90</sub>Fe<sub>10</sub> alloy (wt%,  $1319 \text{ MPa}\cdot\mu\text{m}^{1/2}$ ) [31]. The  $\Delta\sigma_{ppt}$  can be estimated using the Orowan mechanism by [32]:

Fig. 5 SEM images showing fractured surfaces of the a CF and b, c CFZ alloys. d EDS maps in the region of c



$$\Delta\sigma_{ppt} = M \frac{0.4Gb \ln(2\bar{r}/b)}{\pi\lambda \sqrt{1-\nu}}, \quad (3)$$

where  $M$  is the Taylor factor (3.06 for FCC materials [33]),  $G$  is the shear modulus (48 GPa for pure Cu [34]),  $b$  is the Burgers vector of the Cu-rich phase [0.256 nm obtained from the XRD patterns in Fig. 2a], and  $\nu$  is the Poisson's ratio (0.35 for pure Cu [35]). The terms,  $\lambda$  and  $\bar{r}$ , in Eq. (3) represent the inter-precipitate spacing and the mean radius of a circular cross-section for a spherical precipitate, respectively, calculated as follows:

$$\lambda = 2\bar{r} \left( \sqrt{\frac{\pi}{4f_{ppt}}} - 1 \right), \quad (4)$$

$$\bar{r} = r \sqrt{\frac{2}{3}}, \quad (5)$$

where  $f_{ppt}$  and  $r$  are the fraction and mean radius of precipitates, respectively. In the present study, the morphology of Fe<sub>2</sub>Zr precipitates was assumed to be spherical, and the  $r$  was approximated to ~700 nm using the equivalent radius. Thus, using Eqs. (2) and (3), the estimated  $\Delta\sigma_{gb}$  and  $\Delta\sigma_{ppt}$  are 180 MPa and 15 MPa, respectively, where the summation of  $\Delta\sigma_{gb}$  and  $\Delta\sigma_{ppt}$  is close to the difference in yield strength between two alloys (~203 MPa). Notably, the  $\Delta\sigma_{gb}$  is much higher than the  $\Delta\sigma_{ppt}$ . Since the  $\Delta\sigma_{gb}$  is associated with the grain size difference caused by the Zener pinning effect, the Fe<sub>2</sub>Zr precipitates contribute to the strengthening of the CFZ alloy through grain refinement and precipitation hardening.

## 4 Conclusions

In this work, we studied the evolution of microstructure and mechanical properties of Cu<sub>60</sub>Fe<sub>40</sub> (wt%) alloys with and without Zr element. It has been demonstrated that the liquid–liquid phase separation of the Cu–Fe system is inhibited by the addition of Zr. The dual-phase microstructure with Cu-rich and Fe-rich phases is observed in both Zr-free and Zr-containing alloys. A slight variation in the distribution of Fe content during solidification leads to changes in the phase fraction and precipitation behavior of the Zr-containing alloy. The formation of Fe<sub>2</sub>Zr-type precipitates in the Zr-containing alloy gives rise to grain refinement through the Zener pinning effect. Although the tensile elongation of the Zr-containing alloy decreases, the strength of the alloy is significantly improved through strengthening induced by grain boundaries and precipitates. We believe that these findings may provide a pathway for future development of Cu–Fe–Zr system.

**Acknowledgements** This work was supported by the National Research Foundation of Korea (NRF) grant funded by the Korea government (MSIT) (NRF-2022R1A5A1030054). ESK was supported by the Basic Science Research Program through the National Research Foundation of Korea (NRF) funded by the Ministry of Education (2022R1A6A3A13073830). JM acknowledged the support from the Basic Science Research Program through the National Research Foundation of Korea (NRF), funded by the Ministry of Education (2021R1A6A3A03044109). YTC was supported by the Basic Science Research Program “Fostering the Next Generation of Researcher” through the NRF funded by the Ministry of Education (2022R1A6A3A13073824).

## Declarations

**Conflict of Interest** The authors declare that they have no conflict of interest.

## References

1. J. Moon, J.M. Park, J.W. Bae, H.-S. Do, B.-J. Lee, H.S. Kim, *Acta Mater.* **193**, 71 (2020)
2. R.P. Shi, C.P. Wang, D. Wheeler, X.J. Liu, Y. Wang, *Acta Mater.* **61**, 1229 (2013)
3. L. Qu, E. Wang, K. Han, X. Zuo, L. Zhang, P. Jia, J. He, *J. Appl. Phys.* **113**, 173708 (2013)
4. H. Fernee, J. Nairan, A. Atrens, *J. Mater. Sci.* **36**, 2711 (2001)
5. C. Zhang, C. Chen, L. Huang, T. Lu, P. Li, W. Wang, F. Yang, A.A. Volinsky, Z. Guo, *Powder Metall.* **64**, 308 (2021)
6. X. Luo, D. Yuan, H. Wang, H. Chen, X. Xiao, B. Han, H. Huang, B. Yang, *J. Magn. Magn. Mater.* **556**, 169407 (2022)
7. R.D. Noce, O.D.M. Gomes, S.D. de Magalhães, W. Wolf, R.B. Guimarães, A.C. de Castro, M.J.M. Pires, W.A.A. Macedo, D. Givord, V.M.T.S. Barthem, *J. Appl. Phys.* **106**, 093907 (2009)
8. S. Mishra, P.A. Beck, *Phys. Status Solidi A* **19**, 267 (1973)
9. C. Biselli, D.G. Morris, *Acta Mater.* **44**, 493 (1996)
10. E. Büyükkayacı, İ Şimşek, D. Özyürek, *Met. Mater. Int.* **27**, 4618 (2021)
11. H. Gao, J. Wang, D. Shu, B. Sun, *Scripta Mater.* **53**, 1105 (2005)
12. C.P. Wang, X.J. Liu, I. Ohnuma, R. Kainuma, K. Ishida, *Science* **297**, 990 (2002)
13. X.Y. Lu, C.D. Cao, M. Kolbe, B. Wei, D.M. Herlach, *Mater. Sci. Eng. A* **375–377**, 1101 (2004)
14. Z. Yang, Q. Jin, *Mater. Res. Express* **9**, 056514 (2022)
15. S. Kloos, M.A. Dechet, W. Peukert, J. Schmidt, *Powder Technol.* **335**, 275 (2018)
16. A. Chatterjee, E. Sprague, J. Mazumder, A. Misra, *Mater. Sci. Eng. A* **802**, 140659 (2021)
17. S.B. Luo, W.L. Wang, J. Chang, Z.C. Xia, B. Wei, *Acta Mater.* **69**, 355 (2014)
18. Z. Sun, X. Song, Z. Hu, S. Yang, G. Liang, J. Sun, *J. Alloy. Compd.* **319**, 266 (2001)
19. Y.H. Wu, W.L. Wang, J. Chang, B. Wei, *J. Alloy. Compd.* **763**, 808 (2018)
20. J. He, J.-Z. Zhao, X.-F. Wang, L.-L. Gao, *Metall. Mater. Trans. A* **36**, 2449 (2005)
21. H.-J. Moon, T.-M. Yeo, S.H. Lee, J.-W. Cho, *Scripta Mater.* **205**, 114218 (2021)
22. H. Okamoto, *J. Phase Equilib. Diffus.* **33**, 417 (2012)
23. D. Arias, J.P. Abriata, *Bull. Alloy Phase Diagr.* **9**, 597 (1988)
24. G. Kurdjumov, G. Sachs, *Z. Physik* **64**, 325 (1930)
25. Z. Nishiyama, *Sci. Rep. Tohoku Imp. Univer.* **23**, 637 (1934)
26. G. Wassermann, *Arch. Eisenhüttenwes.* **16**, 647 (1933)

27. F. Stein, G. Sauthoff, M. Palm, J. Phase Equilib. **23**, 480 (2002)
28. Y. Guan, Y. Liu, Z. Ma, H. Li, H. Yu, Met. Mater. Int. **28**, 1488 (2022)
29. M. Eftekhari, G. Faraji, M. Bahrami, M. Baniassadi, Met. Mater. Int. **28**, 1725 (2022)
30. B. Fu, C. Pei, H. Pan, Y. Guo, L. Fu, A. Shan, Mater. Res. Express **7**, 116516 (2020)
31. Y. Li, D. Yi, J. Zhang, J. Alloy. Compd. **647**, 413 (2015)
32. J. Moon, E. Tabachnikova, S. Shumilin, T. Hryhorova, Y. Estrin, J. Brechtel, P.K. Liaw, W. Wang, K.A. Dahmen, A. Zargar, J.W. Bae, H.-S. Do, B.-J. Lee, H.S. Kim, Mater. Today **50**, 55 (2021)
33. E.A. Eid, M.M. Sadawy, Met. Mater. Int. **27**, 4536 (2021)
34. S. Shakibhamedan, S. Sheibani, A. Ataie, Met. Mater. Int. **27**, 4271 (2021)
35. H.M. Ledbetter, E.R. Naimon, J. Phys. Chem. Ref. Data **3**, 897 (1974)

**Publisher's Note** Springer Nature remains neutral with regard to jurisdictional claims in published maps and institutional affiliations.

Springer Nature or its licensor holds exclusive rights to this article under a publishing agreement with the author(s) or other rightsholder(s); author self-archiving of the accepted manuscript version of this article is solely governed by the terms of such publishing agreement and applicable law.